Standard and nonstandard nematic electrohydrodynamic convection in the presence of asymmetric ac electric fields

Jonathan Low* and S. John Hogan
Department of Engineering Mathematics, University of Bristol, Queen's Building, Bristol BS8 1TR, United Kingdom
(Received 23 April 2008; published 16 October 2008)

In planar nematic electrohydrodynamic convection (EHC), a microscopic liquid crystal cell is driven by a homogeneous ac electric field, which, if strong enough, causes the fluid to destabilize into a regular pattern-forming state. We consider asymmetric electric fields $E(t)=E(t+T)\neq -E(t+T/2)$, which leads to the possibility of three different types of instabilities at onset: conductive, dielectric, and subharmonic. The first two are already well known as they are easily produced when the system is driven by symmetric electric fields; the third can only occur when the electric field symmetry is broken. We present theoretical results on EHC using linear stability analysis and Floquet theory. We consider rigid and free boundary conditions, extending the model to two Fourier modes in the vertical plane, the inclusion of flexoelectricity, and using standard (nematic electric conductivity $\sigma_a>0$ and dielectric anisotorpy $\epsilon_a<0$) and nonstandard ($\sigma_a<0$) material parameters. We make full use of a three-dimensional linear model where two mutually perpendicular planar wave numbers q and p can be varied. Our results show that there is a qualitative difference between the boundary conditions used, which is also dependent on how many vertical Fourier modes were used in the model. We have obtained threshold values favoring oblique rolls in subharmonic and dielectric regimes in parameter space. For the nonstandard EHC parameter values, both conduction and subharmonic regimes disappear and only the dielectric threshold exists.

DOI: 10.1103/PhysRevE.78.041706 PACS number(s): 61.30.Gd, 47.54.−r, 64.70.M−

I. INTRODUCTION

Planar nematic electrohydrodynamic convection (EHC) is an example of a pattern-forming system where a nematic liquid crystal confined in a cell of microscopic thickness is driven out of equilibrium by a vertically applied electric field. Above a certain electric field amplitude, the basic state of the liquid crystal destabilizes into regular roll patterns. These will be dynamic in nature under an ac electric field. Such a system is popular with experimentalists because of the ease of control of the external parameters and the observation of the transition between pattern states. Examples of such parameters are liquid crystal temperature and the frequency and type of applied electric field. An in-depth introduction and review into pattern formation in liquid crystals can be found in Buka and Kramer [1] and Buka *et al.* [2,3].

For standard nematic EHC, a liquid crystal must have its conductive anisotropy σ_a positve and its dielectric anisotropy ϵ_a negative. This has been the *de facto* standard for EHC studies and has been extensively covered in both theoretical and experimental studies where the Carr-Helfrich mechanism [4,5] for instability is employed. The first such studies under time-dependent electric fields go back to de Gennes, Dubois-Violette, and Parodi [6] where two types of instabilities, conductive and dielectric, were discovered depending on the frequency of the ac field. The transition from conductive to dielectric patterns occurs at a particular frequency value f_c. Dubois-Violette carried out a further study under square-wave and sinusoidal fields [7] and a more analytical study was done for the symmetric field case [8]. Krekhov *et al.* have recently looked at the situation where the value of σ_a changes sign [9]. In the standard theoretical model, no instability occurs unless flexoelectricity is included in the model, which then becomes the main mechanism for instability.

In this paper we focus on results obtained when applying an asymmetric electric field to the cell. John and Stannarius [10] were the first to demonstrate that an electric field which did not have the symmetric property $E(t)=-E(t+T/2)$ can cause the first pattern transition to consist of T-antiperiodic pattern dynamics in certain areas of parameter space, rather than the usual T-periodic conductive and dielectric regimes. More interesting was the fact that such an electric field turns out to be a necessary but not a sufficient condition for the bifurcation to be of this type [10,11]; conductive and dielectric dynamic instabilities are possible with such asymmetric fields. From a mathematical perspective, a linear stability analysis can determine the type of onset pattern by calculating the Floquet multipliers of the linearized system. If the largest multiplier passes +1, the onset pattern is conductive or dielectric. Passing through −1 gives a subharmonic bifurcation.

In this paper we extend the work of John and Stannarius [10]. The next section presents the equations on which the theoretical analysis is based, which includes extending the two-dimensional (2D) linear model that they have used. Here we move to the 3D model, using rigid boundary conditions and the inclusion of flexoelectricity. Section III covers the results of our theoretical analysis. In the first part, we show the qualitative and quantitative difference between free and rigid boundary conditions, the 2D and 3D models, and using one and two vertical Fourier modes. The second part of Sec. III deals with the threshold curves and dynamics in the nonstandard electroconvection scenario, using both symmetric square-wave and asymmetric piecewise constant electric fields. Section IV summarizes the results, together with a conclusion.

*j.low@bristol.ac.uk

 ©2008 The American Physical Society

II. GOVERNING EQUATIONS

A nematic cell is modeled by an infinitely extended horizontal plane parallel to the x-y axes with boundaries equidistant from the plane at $z=0$ with a thickness d in order of micrometres. The homogeneous applied electric field $E(t)$ acts parallel to the z axis. The governing equations are the Ericksen-Leslie[1] dynamic equations [12], which describe the linear and angular momentum of the nematic director field $\mathbf{n}(\mathbf{x},z,t)$, the poloidal and toroidal velocity potentials $f(\mathbf{x},z,t)$ and $g(\mathbf{x},z,t)$, respectively, together with the quasistatic Maxwell's equations describing the electric potential $\phi(\mathbf{x},z,t)$. Here, $\mathbf{x}=(x,y)$ describes the Cartesian plane parallel to the electrode plates. The full linear equations are given in Appendix B.

Rather than writing out the detailed derivation leading to the linearized system of equations, we focus on the mathematical approach we take here in comparison to the theoretical models used by Stannarius and co-workers and Pesch and co-workers.

A. Adiabatic approximation

Physically, the adiabatic approximation assumes that the inertia of the system is negligible compared to the viscous forces. Hence the equations are derived in the viscous limit of hydrodynamics where the nondimensionalized mass density term is set to zero and this allows further simplification of the system by eliminating both velocity variables and ending up with a set of ordinary differential equations (ODEs) implicit in f and g. This approximation is very good for two reasons. The first is that the difference of the resulting Floquet multipliers of the linearized system is negligible, of the order of 10^{-3}. The second is of practical importance in calculating the Floquet multipliers and the periodic solutions at onset with the current numerical code we have. Without this approximation, one is left with an ODE system where the velocity potentials f and g jump sharply at the points where the applied ac electric field changes value. As a consequence, MATLAB's built-in ode45 solver fails to compute a numerical solution. This approximation gets around this difficulty. It is worth mentioning that several published papers use this approximation where this leads to the derivation of a 2×2 system of ODEs [6,8,10,11,13,14] consisting of the charge density[2] ρ_e and the n_z director deflection in a 2D setting.

B. Nondimensionalization

We apply the nondimensionalization scheme [9,15,16] to the set of linearized equations, resulting in two nondimensionalized parameters of the system,

$$R=\left(\frac{V_{\mathrm{app}}}{V_0}\right)^2, \quad Q=\frac{\sigma_0\alpha_0 d^2}{\epsilon_0 K_0 \pi^2}, \tag{1}$$

where R is a measure of the amplitude of the applied electric field on the system. Referring to Fig. 1, the asymmetric field

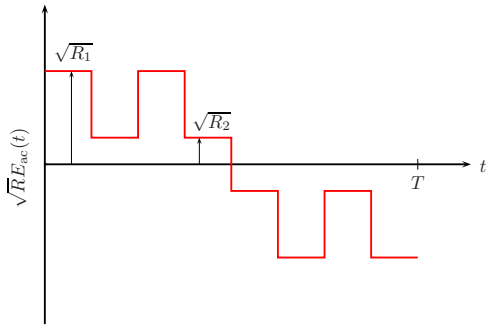

FIG. 1. (Color online) One full period of the nondimensionalized wave form of $E(t)=V(t)/d=(V_{\mathrm{app}}/d)E_{\mathrm{ac}}(t)=(V_0/d)\sqrt{R}E_{\mathrm{ac}}(t)$, where V_{app} is the amplitude of the applied voltage. The nondimensional time period is $T=1/(f_q\tau_{\mathrm{DD}})$, where f_q is the frequency of $E(t)$.

is a superposition of a low-frequency square wave with amplitude R_l and another which has 4 times its frequency and an amplitude R_h. This frequency ratio of 1:4 remains fixed throughout this paper. The voltages are related by $V_{(l/h)}=V_0\sqrt{R_{(l/h)}}$, and V_{app} takes V_l or V_h as appropriate. The values R_1 and R_2 are given as

$$R_1=R_l+R_h+2\sqrt{R_lR_h}, \tag{2}$$

$$R_2=R_l+R_h-2\sqrt{R_lR_h}. \tag{3}$$

When we use these asymmetric fields in our calculations, both R_l and R_h are the parameters we vary. For calculations involving symmetric fields, amplitude R and field frequency are the changing parameters. The other nondimensional number Q is a measure of the charge relaxation time to director relaxation time ratio. The time variable is nondimensionalized using τ_{DD} which is the director-diffusion time [15].

C. Vertical fourier modes and boundary conditions

In this paper, we present results which use both free and rigid boundary conditions. The former is numerically easy to implement, but are unrealistic since the no slip condition does not hold. The latter requires the governing equations for the poloidal velocity potential f to be coupled with Chandrasekhar functions [17]. In both cases, we use the "planar" alignment configuration where the nematic director $\mathbf{n}$ is strongly anchored parallel to the boundaries.

The free boundary conditions are given, in nondimensional form, as

$$\mathbf{n}(z=\pm\pi/2)=(1,0,0),$$

$$\phi(z=\pm\pi/2)=g(z=\pm\pi/2)=0,$$

$$f(z=\pm\pi/2)=\partial_z^2 f(z=\pm\pi/2)=0.$$

They can be satisfied by using the sine ansatz for all variables: namely,

$$S_1(z)=\sin(z+\pi/2) \quad \text{for the first } z \text{ mode}, \tag{4}$$

[1]Some papers refer to it as the Navier-Stokes equations along with the stress tensor for nematic liquid crystals containing the Leslie viscosities α_i.

[2]Electric potential ϕ and charge density ρ_e and related via Maxwell's equations [Eq. (B5)] with Eq. (B12).

$$S_2(z) = \sin(2[z + \pi/2]) \quad \text{for the second } z \text{ mode}. \tag{5}$$

For the rigid boundary conditions

$$\mathbf{n}(z = \pm \pi/2) = (1,0,0),$$

$$\phi(z = \pm \pi/2) = g(z = \pm \pi/2) = 0,$$

$$f(z = \pm \pi/2) = \partial_z f(z = \pm \pi/2) = 0,$$

the first derivative of the velocity potential f can be satisfied by using the orthogonal Chandrasekhar basis functions which form a vector space. The first mode is the leading even function

$$C_1(z) = \frac{1}{\sqrt{2}}\left(\frac{\cosh(\mu_1 z)}{\cosh\left(\frac{\pi}{2}\mu_1\right)} - \frac{\cos(\mu_1 z)}{\cos\left(\frac{\pi}{2}\mu_1\right)}\right), \tag{6}$$

and the second mode is the leading odd function

$$C_2(z) = \frac{1}{\sqrt{2}}\left(\frac{\sinh(\nu_1 z)}{\sinh\left(\frac{\pi}{2}\nu_1\right)} - \frac{\sin(\nu_1 z)}{\sin\left(\frac{\pi}{2}\nu_1\right)}\right), \tag{7}$$

where $\mu_1 = 1.505\,62$ and $\nu_1 = 2.499\,75$, which satisfy the condition $\partial_z C_1(\pm\pi/2) = \partial_z S_1(\pm\pi/2) = 0$. Here the functions are normalized such that

$$\frac{2}{\pi}\int_{-\pi/2}^{\pi/2} C_1(z)C_1(z) = 1,$$

$$\frac{2}{\pi}\int_{-\pi/2}^{\pi/2} C_1(z)C_2(z) = 0.$$

One of our models uses the first two modes for each variable. The leading mode approximation is also used in this paper for the purpose of showing the quantitative difference between free and rigid boundary conditions for one set of results. Examples of threshold curves using both types of boundary conditions separately under a sinusoidal driving electric field can be found in Bodenschatz *et al.* [18].

D. ODE system

Using two z modes and representing the planar fluctuations as horizontal complex Fourier modes, the perturbations to the basic state take the form

$$f(\mathbf{x},z,t) = f_1(t)\exp(i\mathbf{q}\cdot\mathbf{x})S_1(z) + f_2(t)\exp(i\mathbf{q}\cdot\mathbf{x})S_2(z) \tag{8}$$

for each of the variables where $\mathbf{q} = (q,p)$ is the wave-number vector. For rigid boundary conditions, the velocity f takes the alternative form

$$f(\mathbf{x},z,t) = f_1(t)\exp(i\mathbf{q}\cdot\mathbf{x})C_1(z) + f_2(t)\exp(i\mathbf{q}\cdot\mathbf{x})C_2(z), \tag{9}$$

while the remaining variables take the form of Eq. (8). Substituting the ansatz into the governing equations, linearizing about the basic state, and applying the adiabatic approximation results in a 6×6 ODE matrix system, which takes the canonical form

$$\mathcal{B}_0(t;R)\partial_t \mathbf{V}_0(t) = \mathcal{L}_R(t;R,Q)\mathbf{V}_0(t), \tag{10}$$

where $\mathbf{V}_0(t) = [\phi_1(t), \phi_2(t), n_{y1}(t), n_{y2}(t), n_{z1}(t), n_{z2}(t)]$ and some of the matrix coefficients depend on time. For the one-z-mode model, the system reduces to 3×3 with $\mathbf{V}_0(t) = [\phi_1(t), n_{y1}(t), n_{z1}(t)]$. The one-mode 2×2 1D and 2D versions have been studied before [6,10,13]. The coefficients of $\mathcal{B}_0(t;R)$ and $\mathcal{L}_R(t;R,Q)$ contain numerical values as a result of projecting the equations onto the z modes. For free boundary conditions, they either take the value 1 or -1 after normalization, whereas for rigid boundary conditions they take various numerical values since the sine and Chandrasekhar functions are not orthogonal: i.e.,

$$\int_{-\pi/2}^{\pi/2} C_1(z)S_1(z)dz \neq 0. \tag{11}$$

The explicit form of Eq. (10) can be found in the Appendix of papers by Kaiser and Pesch [16] and Krekhov *et al.* [9]. However, for completeness, the full linear equations are reproduced in Appendix B, which includes the finer details such as viscosity combination terms, the explicit values when the ODEs are projected onto the z modes, and the differences between the one- and two-z-mode models.

Notice that we do not break the time dependence into its Fourier modes. An example where Fourier modes in time are used in EHC can be found in Bodenschatz *et al.* [18], but here we solve the ODE system forward in time over one or two periods of the electric field cycle. For the purpose of finding the Floquet multipliers, we take advantage of the piecewise constant form of the electric field and calculate the eigenvalues of the resulting chain of matrix exponentials. For square waves it is

$$\boldsymbol{V}_0(nT) = [\underline{\mathbf{S}}^{(-)}\underline{\mathbf{P}}^{(-)}\underline{\mathbf{S}}^{(+)}\underline{\mathbf{P}}^{(+)}]^n \boldsymbol{V}_0(0), \tag{12}$$

and for the asymmetric electric wave forms it is

$$\boldsymbol{V}_0(nT) = \mathcal{P}^n \boldsymbol{V}_0(0), \tag{13}$$

where

$$\mathcal{P} = \underline{\mathbf{S}}^{\mathrm{E}}\underline{\mathbf{A}}_2\underline{\mathbf{S}}^{\mathrm{M}}\underline{\mathbf{A}}_1, \tag{14}$$

with

$$\underline{\mathbf{A}}_1 = \underline{\mathbf{P}}^{(+-)}\underline{\mathbf{S}}^{(++)}\underline{\mathbf{P}}^{(++)}\underline{\mathbf{S}}^{(+-)}\underline{\mathbf{P}}^{(+-)}\underline{\mathbf{S}}^{(++)}\underline{\mathbf{P}}^{(++)} \tag{15}$$

and

$$\underline{\mathbf{A}}_2 = \underline{\mathbf{P}}^{(--)}\underline{\mathbf{S}}^{(-+)}\underline{\mathbf{P}}^{(-+)}\underline{\mathbf{S}}^{(--)}\underline{\mathbf{P}}^{(--)}\underline{\mathbf{S}}^{(-+)}\underline{\mathbf{P}}^{(-+)}. \tag{16}$$

The $\underline{\mathbf{S}}$ matrices relate to the fact that the electric potential ϕ is discontinuous as a result of the jumps in the electric field and the $\underline{\mathbf{P}}$ matrices are the calculated matrix exponentials. These can be worked out in Appendix C, including the terms $\underline{\mathbf{S}}^{\mathrm{M}}$ and $\underline{\mathbf{S}}^{\mathrm{E}}$, which just involve E_{ac} changing sign in the middle and at the end of the time period T, respectively.

E. Scenario settings

There are already calculated threshold curves in the asymmetric electric field case in two dimensions (excluding the y

coordinate) using one z mode without flexoelectricity [10] which we repeat here for completeness. First we calculate the threshold curves using rigid boundary conditions and the same Mischung V material parameters under the following conditions separately: (a) 2D using one z mode without flexoelectricity, (b) 3D (wave number p can vary) using one z mode without flexoelectricity, (c) 3D using using one z mode with flexoelectricity, (d) 3D using two z modes without flexoelectricity, and (e) 3D using two z modes with flexoelectricity.

The asymmetric electric field used in the scenarios above is a superposition of two square waves, one with 80 Hz frequency and amplitude R_l and the other is a 320-Hz wave with amplitude R_h. The results of these calculations are presented and compared in Sec. III A. For nonstandard EHC, the first thing we did was to repeat the threshold results [15] using 4–methoxybenzylidene-4'-butylaniline (MBBA) parameters and show the differences between our results and theirs. We would expect some differences since we are using a square-wave rather than a sinusoidal electric field and, as mentioned before, we do not solve the system using a Fourier series in time and we limit our model to two z modes. The main point here is that we are on the lookout for the existence of threshold curves when $\sigma_a<0$ using our model. From there on, we calculate the threshold curves using the asymmetric field, varying σ_a in the same way as we did for the symmetric field case. In addition, we look at the cases with and without flexoelectricity separately to see if electrohydrodynamic instability can be achieved purely by the asymmetric field influence. We construct the asymmetric electric field by superimposing two square waves with 20 and 80 Hz frequencies and use this for calculations involving MBBA parameters, in order to capture the possible subharmonic behavior.

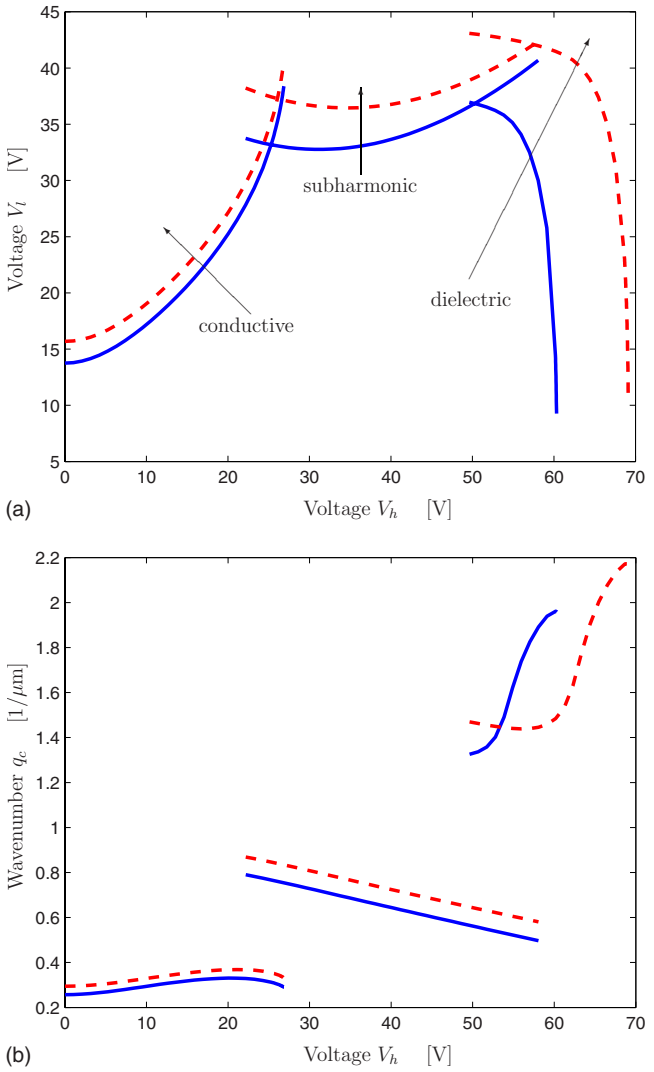

FIG. 2. (Color online) (a) Threshold curves and (b) corresponding critical q_c wave numbers for Mischung V under the one-z-mode model using both free (solid line) and rigid (dashed line) boundary conditions.

III. RESULTS

A. Standard EHC with Mischung V using free and rigid boundary conditions

Figure 2(a) shows the calculated threshold using the leading z-mode approximation, and Fig. 2(b) shows the corresponding wave numbers. The results for free boundary conditions are exactly the values found by John and Stannarius [10]. As expected, this shows the quantitative difference between the free and rigid boundary conditions, but we were surprised at first that the threshold boundary moved away from the experimental data [10] (not shown here but very close to the free boundary curve). The rigid boundary threshold curve would be the starting point in attempting to match the theoretical and experimental results. The calculation was repeated, this time allowing for the wave number p to vary. The optimal wave-number vector $\mathbf{q}=(q_c,p_c)$ turns out to be normal roll formation with $p_c=0$ everywhere. To check this was true, the calculations were repeated, this time with the second z Fourier mode included. The resulting curves for rigid boundary conditions with and without flexoelectricity[3] are shown in Figs. 3–5. Here we see that, with or without flexoelectricity, the conductive and dielectric areas do indeed favour normal rolls, but the subharmonic regime favors patterns with a nonzero p_c wave number. The critical threshold plots suggest that flexoelectricity is not a crucial factor in triggering conductive and subharmonic instabilities as their respective curves are very close to each other. But we see that it does significantly affect the dielectric regime, where we believe the director fluctuations amplify the flexoeffect through Eq. (B12). Looking at the critical wave numbers in Figs. 4 and 5, their magnitudes appear similar in each instability regime; however, the angle $\alpha=\arctan(p_c/q_c)$ becomes nonzero (approximately 10° on average) in the subharmonic regime. This would seem to confirm the normal rolls observed in John and Stannarius's experiment [10], but looking

[3]For the calculation with the flexoeffect, e_1 and e_3 were simply given the same values as MBBA as a first try.

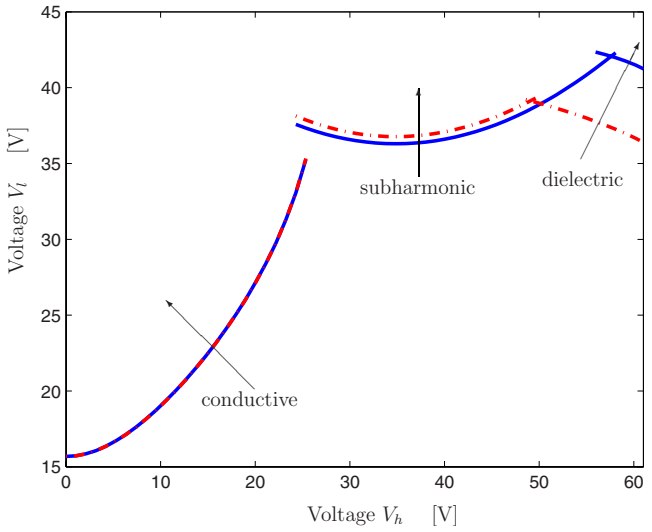

FIG. 3. (Color online) Threshold curves for Mischung V using the full two-z-mode 3D model. The solid lines are the calculated values without flexoelectricity; the dashed lines are those with flexoelectricity.

at Fig. 2(d) in that paper, the rolls do appear to be slightly out of alignment with the y axis. In Fig. 5, if one extended the nonzero α dotted line (the subharmonic case) towards the $V_h=50-60$ V range, there exists a crossover point from oblique to normal rolls in the case with flexoelectricity, which happens at around $V_h=52$ V, but will not happen practically since this parameter area would be covered by the dielectric instability which would be observed instead.

Time-periodic solutions

Here we show two examples of the time-periodic solutions at onset in the subharmonic regime. These are exactly the eigenvectors associated with the Floquet multipler −1. Figures 6 and 7 show individually the solutions for the six variables at one particular value of V_h. All subharmonic solutions are T antiperiodic with respect to the driving electric field because the Floquet multiplier is real and hence obeys the odd symmetry of the form $\beta(t+T)=-\beta(t)$. All variables including the electric potential ϕ and director deflections change sign after one period of the driving field and have zero average across two periods. To compare them with Fig. 1, the time period is $T=1/(f_q\tau_{DD})=0.3027$.

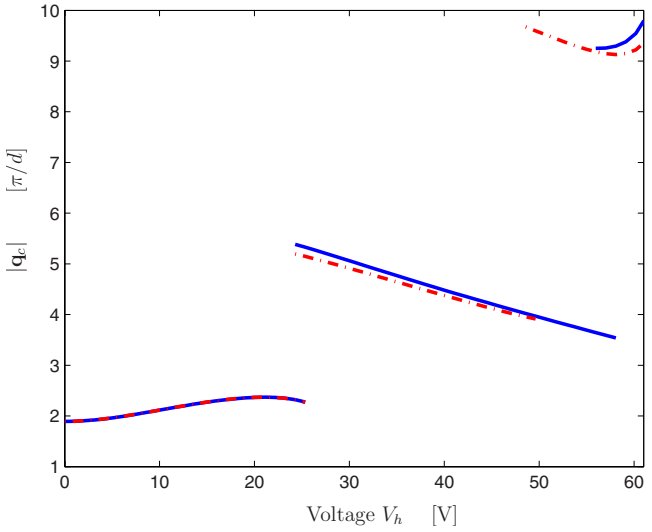

FIG. 4. (Color online) Wave-number magnitudes corresponding to Fig. 3. To compare directly with Fig. 2(b), multiply by π/d.

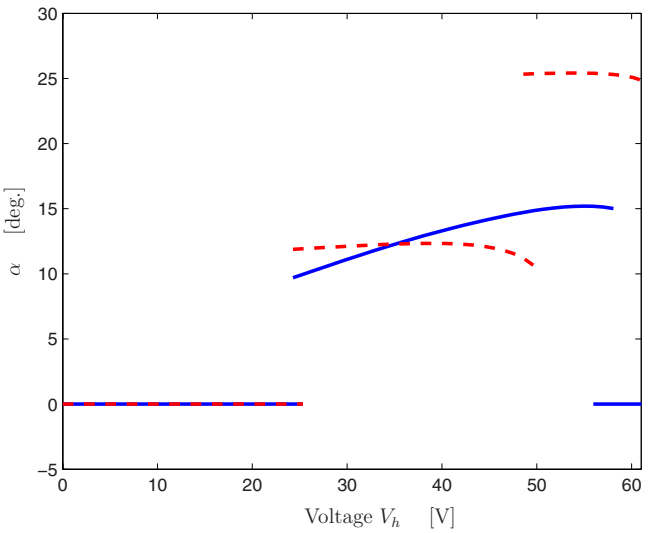

FIG. 5. (Color online) Wave-number angles corresponding to Fig. 4.

B. Nonstandard electroconvection under symmetric square-wave driving

Figures 8–10 show the thresholds and their optimal wave numbers for the case of a planar-aligned nematic cell driven

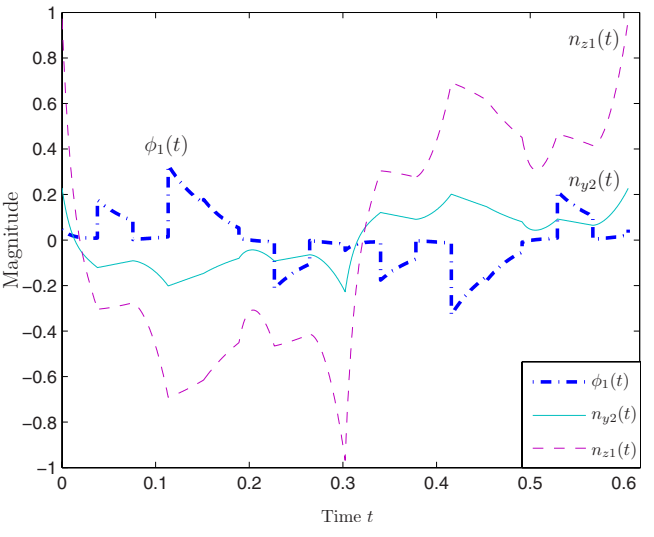

FIG. 6. (Color online) Solution at onset over two time period cycles of the driving electric field at $R_h=30^2$ ($V_h=30V_0=31.6$ V) without flexoelectricity. Only the first leading mode [proportional to $\sin(z+\pi/2)$] exists, which are ϕ_1 and n_{z1}, and only the second mode n_{y2} (proportional to $\sin(2[z+\pi/2])$) exists. The legend is shown in the bottom right-hand corner.

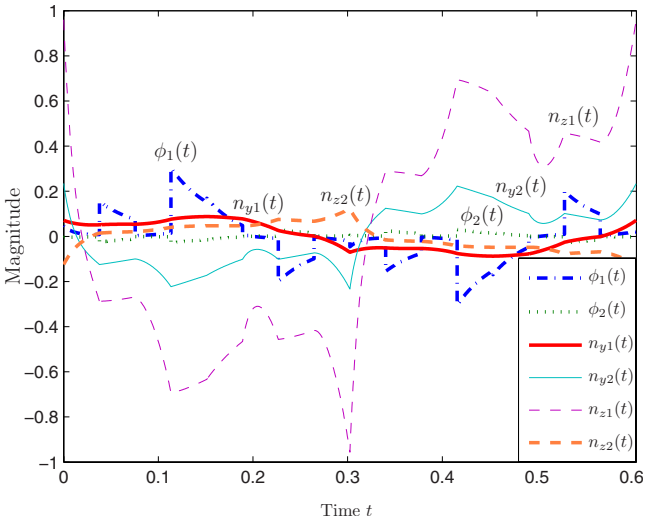

FIG. 7. (Color online) Solution at onset over two time period cycles of the driving electric field with flexoelectricity included in the system at $R_h=30^2$. All individual modes are now nonzero, but the ones that did not exist previously in Fig. 6 appear to be smaller in magnitude. The legend is shown in the bottom right-hand corner.

by a symmetric square-wave field. These have been calculated using the 3D linear model using two z modes with the MBBA parameters [9,19], while the conductive anisotropy σ_a varies. These are similar to the results of Krekhov *et al.* [9] since they used a pure sinusoidal driving field and used many more z modes as well as decomposing the Fourier expansions in time as well. However, our calculations serve two purposes here. First is a check of numerical codes. Second, these results show that it is possible to obtain the nonstandard electroconvection thresholds by the inclusion of just two z modes. One difference the reader may notice straight away is the conduction regime is suppressed sooner as one ramps through the conductive anisotropy value σ_a towards the negative end; the conductive regime area size is already smaller for $\sigma_a=0.5$ and 0.3. It is already suppressed when $\sigma_a=0.1$.

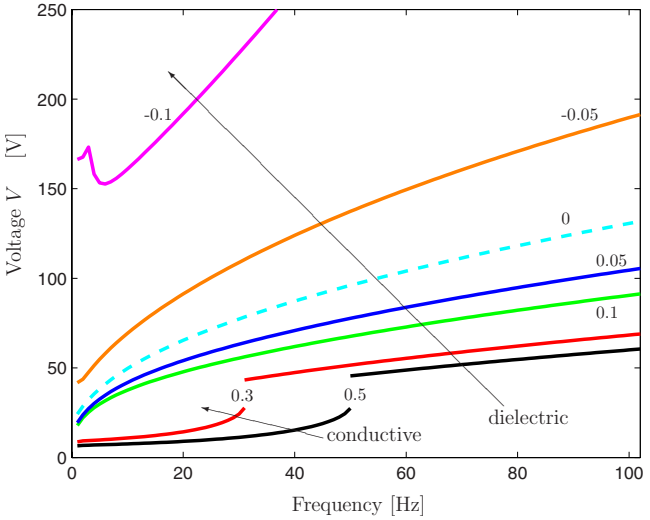

FIG. 8. (Color online) Threshold curves for symmetric square-wave driving on MBBA for various σ_a values.

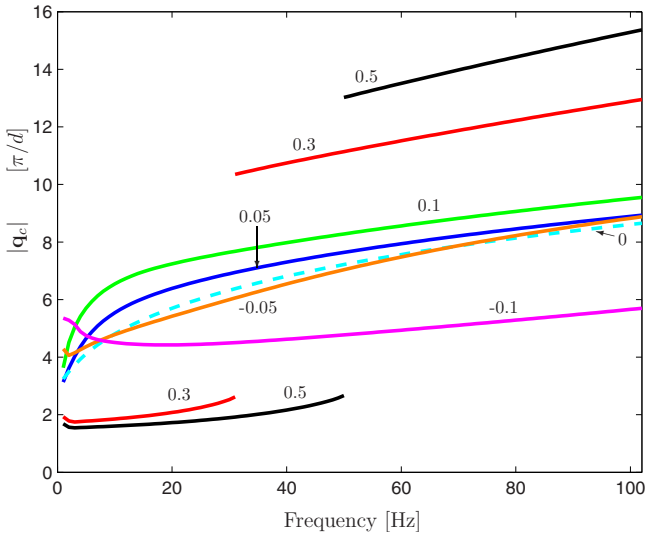

FIG. 9. (Color online) Corresponding wave-number magnitudes to Fig. 8.

C. Nonstandard electroconvection under asymmetric electric fields

Having obtained critical thresholds for nonstandard EHC using two z modes, we then proceed to replace the symmetric driving field with the asymmetric one. For positive $\sigma_a=0.5$ (dashed lines) and 0.3 (dotted lines) in Fig. 11, we obtain the usual shape of the threshold curves across the range of variation of the amplitude voltage of the higher frequency electric field. All three types of instabilities are present, including the subharmonic region. But as σ_a varies from 0.3 to −0.1, both conductive and subharmonic regions disappear and the dielectric instability dominates with much higher threshold values which become independent of the variation of V_h; at these higher values, the asymmetric field nearly becomes a square wave with small fluctuations. Figure 12 shows the critical wave numbers obtained. For σ_a values 0.5 and 0.3,

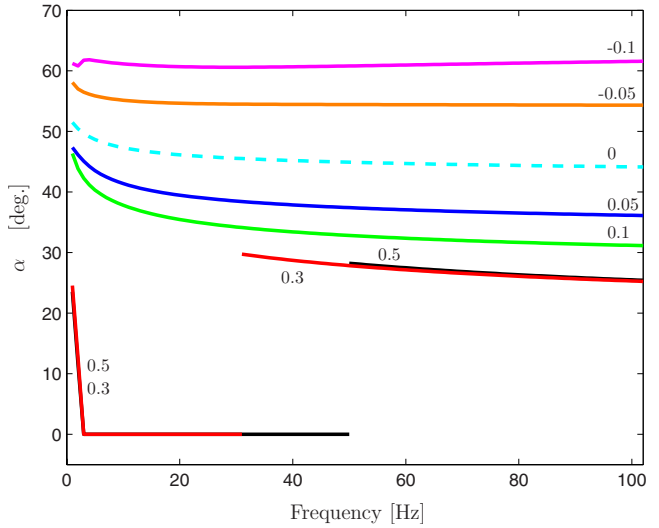

FIG. 10. (Color online) Angle of roll formation in relation to Fig. 9.

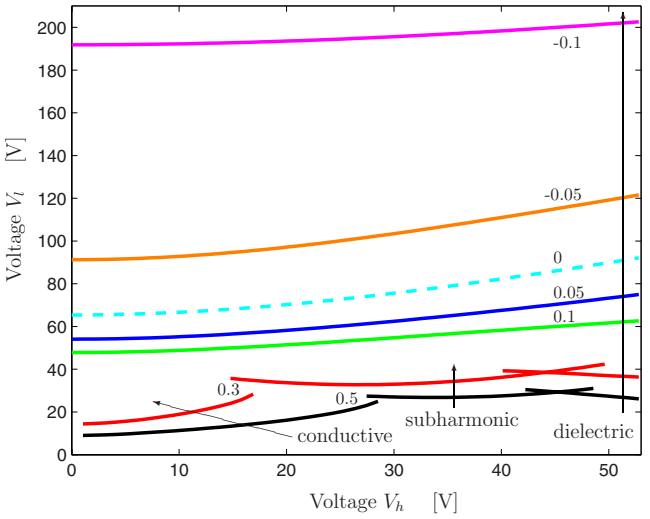

FIG. 11. (Color online) Critical thresholds for the asymmetric driving case with MBBA parameters.

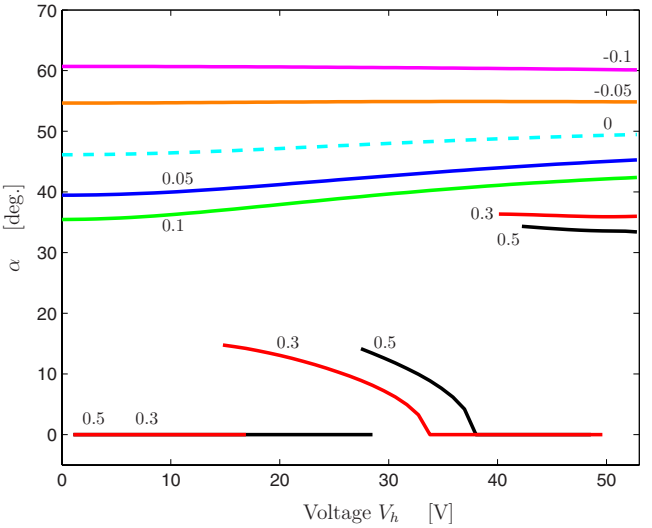

FIG. 13. (Color online) Corresponding angle formation to Fig. 12.

the curves are qualitatively similar to those for Mischung V in Fig. 4. Towards negative σ_a values, the magnitude increases and becomes independent of the amplitude of V_h. The corresponding wave-number angles in Fig. 13 deserve comment. For σ_a taking the values 0.5 and 0.3, the conduction regime consists of normal roll formation, but for both subharmonic and dielectric instabilities, oblique rolls are formed. This is in contrast to Mischung V with flexoelectricity in Fig. 5 where the dielectric regime favors normal rolls. In addition, the crossover from normal to oblique rolls in the subharmonic regime for MBBA changes from one σ_a value to another. Hence it is possible to influence where the crossover happens by altering the material parameters. When σ_a moves towards negative values, the same qualitative behavior follows in that the wave-number magnitude becomes larger and becomes independent of V_h. With a negative or slightly positive σ_a, a nonzero p_c occurs everywhere throughout the voltage range V_h with flexoelectricity coming into play in creating the (dielectric) instability. We performed stability threshold calculations with no flexoeffect ($e_1=e_3=0$). Unfortunately, instability was not found in this case. Krekhov *et al.* explained that if the body force in the Navier-Stokes (or Ericksen-Leslie) equations was out of phase with the driving electric field, then this dampens or suppresses the torque acting on the nematic director, therefore not creating the conditions suitable for electrohydrodynamic convection [9]. This explanation leads to the conclusion that the shape of the field cannot trigger an instability since the body force is itself proportional to the electric field and the sign is governed by the charge density variable ρ_e.

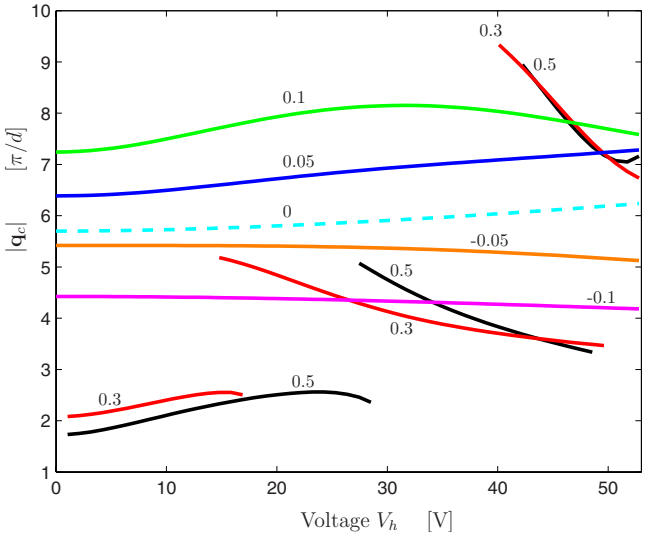

FIG. 12. (Color online) Magnitude of the wave numbers corresponding to Fig. 11.

The onset solutions shown in Figs. 14–16 serve to illustrate the consequence of breaking the electric field symmetry $E(t)=-E(t+T/2)$ and their variation at different values of σ_a. As a consequence, this eliminates the possible mirror and rotational symmetries in the solutions found previously of the form $\beta(t)=\pm\beta(t+T/2)$ for symmetric electric fields, but introduces a new type of solution, subharmonic in nature, where all the variables flip to their negative initial condition values after one period of the driving ac voltage and returning to their original values after another period. Starting at $\sigma_a=0.5$, the solutions show no symmetry between $t=0$ and $t=T$ [$=1/(20\tau_{DD})=0.3085$]. As σ_a becomes negative, the dielectric instability dominates. The symmetry of the form $\beta(t)=\pm\beta(t+T/2)$ is not found exactly, though it does become close as the asymmetric electric field becomes more symmetric at higher values of V_l. Notice that the electric potentials ϕ_1 and ϕ_2 rapidly become negligible as $\sigma_a/\sigma_\perp$ become more negative and the instability becomes dielectric.

The results here show that no subharmonic regime has been found with negative σ_a values. We did try to see if it was possible to obtain instability at negative σ_a values without the flexoeffect and just using the asymmetric field. However, we were unable to get subharmonic solutions with negative σ_a. Hence the subharmonic regime suffers the same fate as the conduction regime where the instability area in the R_l-q plane shrinks in favor of the dielectric regime.

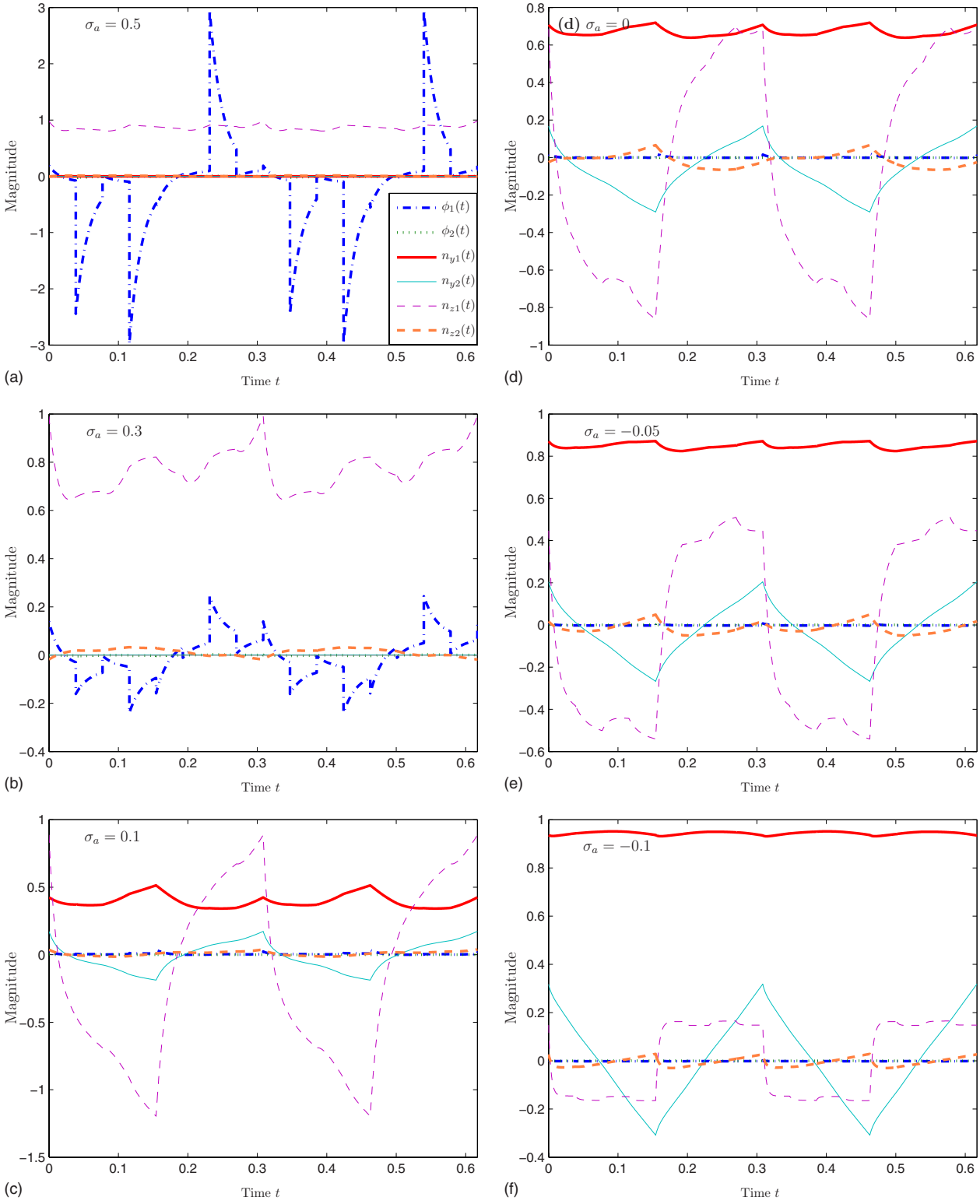

FIG. 14. (Color online) Onset solutions at $R_l=10^2$ for varying σ_a values over two cycles of the driving electric field. The first two are in the conduction regime; the rest are dielectric instabilities. The individual modes $\phi_1(t)$, $\phi_2(t)$, etc., are shown separately in each diagram. The legend is shown in (a).

IV. CONCLUSION AND SUMMARY

The results of standard EHC for Mischung V highlights the differences depending on the detail of the model used. Using the 2D one-z-mode linearized system, the critical threshold lines quantitatively change between using free and rigid boundary conditions as expected; the largest difference is in the subharmonic and dielectric areas of the stability

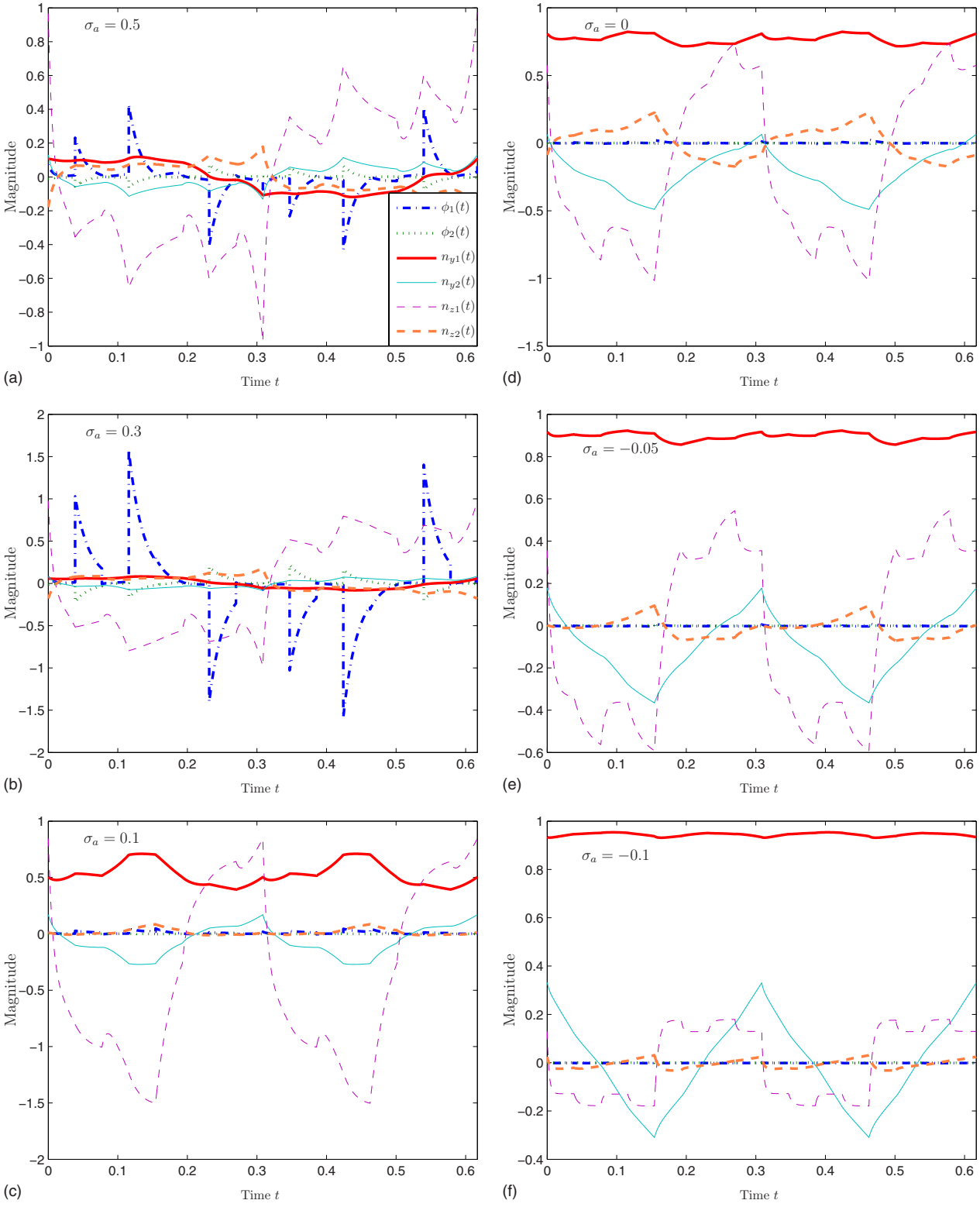

FIG. 15. (Color online) Onset solutions at $R_l=30^2$ for varying σ_a values over two cycles of the driving electric field. The first two are in the subharmonic regime; the rest are dielectric instabilities. The legend is shown in (a).

diagram. Extending the model to 3D (varying p wave number) but keeping one z mode did not change the critical threshold value and normal roll orientation is still preferred. A qualitative difference emerged when the linearized system included the second z Fourier mode in the model. Without flexoelectricity, the result was a nonzero angle formation in the subharmonic regime. When the flexoeffect was included, a crossover point from oblique to normal roll formation emerged in the subharmonic region. It is worth mentioning that the inclusion of the flexoeffect makes little difference in

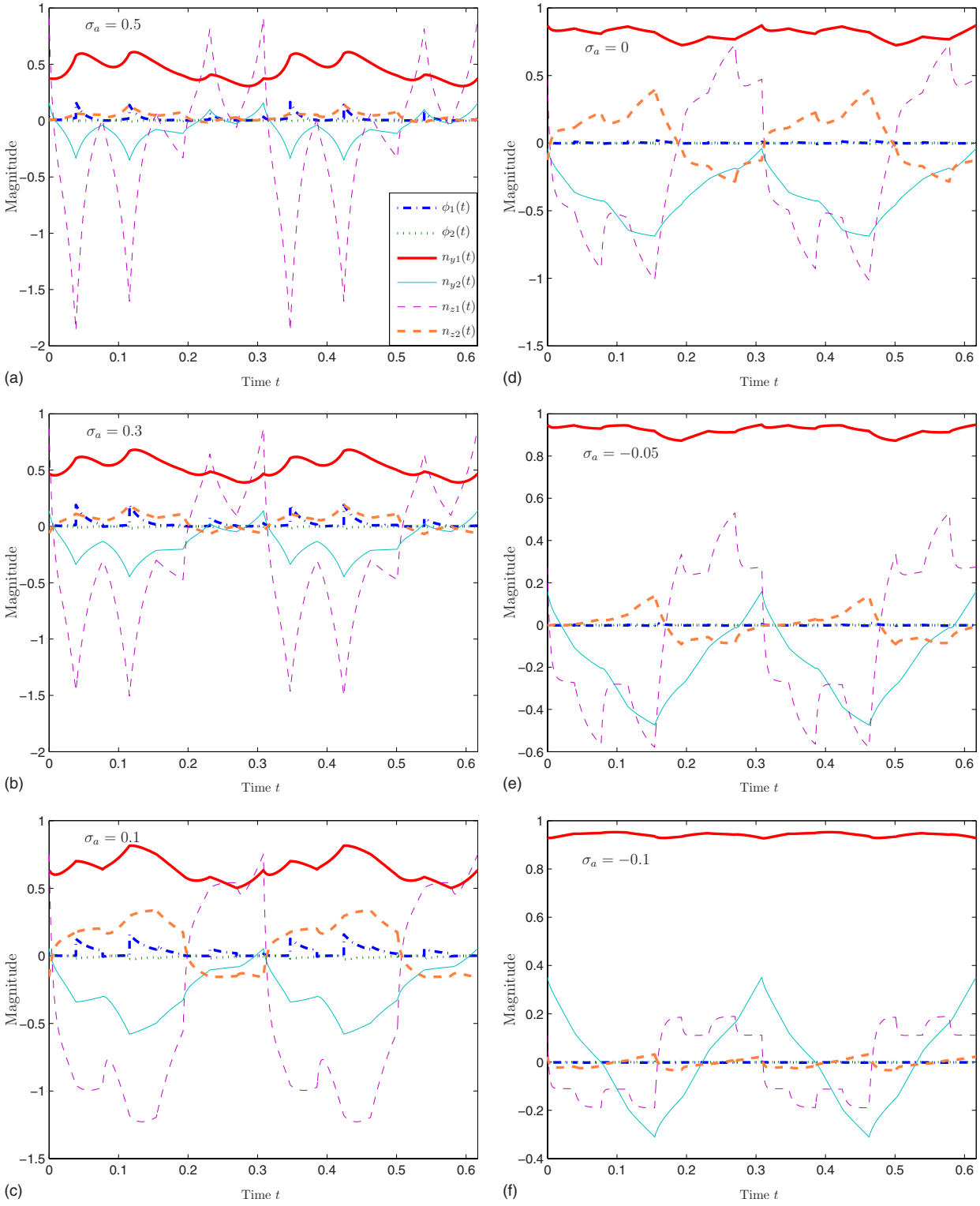

FIG. 16. (Color online) Onset solutions at R_l=50^2 for varying σ_a values over two cycles of the driving electric field. All instabilities are in the dielectric regime. The legend is shown in (a).

the critical thresholds and wave-number magnitudes. Finally, these results would confirm the normal rolls observed in experiments in the conductive and dielectric regimes, but the theory predicts rolls formed at a small tilt angle, 10° on average.

In the scenario of nonstandard EHC with symmetric square-wave driving on MBBA, the results are similar to the calculations by Krekhov *et al.* [9] for a sinusoidal field. This result points out that we still can obtain instability thresholds with the linearized model that only includes the first two

z Fourier modes, albeit with slightly less accuracy compared to a model that includes ten or more. One minor difference is the disappearance of the conductive instability even when σ_a is still positive at the value of 0.1.

The results for nonstandard EHC under an asymmetric driving field reveal the rapid disappearance of the conductive and subharmonic instabilities in favor of the dielectric mode at higher V_h values. From our calculations, the two regions vanish when $\sigma_a=0.1$ or less and the dielectic instability then becomes the only possibility. The calculated wave numbers in Figs. 5 and 12 show that for standard EHC where $\sigma_a>0$, the crossover point from oblique to normal rolls is influenced by the material parameters, including σ_a. As σ_a decreases and becomes negative, both the wave-number magnitude and angle become nearly independent of varying the V_h parameter.[4] The onset solutions of the individual modes $[\phi_1(t), \phi_2(t)$, etc.] have been looked at to observe the symmetry broken as a result of using a field such that $E(t)=E(t+T)\neq -E(t+T/2)$. All modes are T periodic, but T antiperiodic for subharmonic instability. As σ_a decreases toward negative values, the modes start to exhibit some regular pattern in the two halves of the electric field cycle, though no symmetry of the form $\beta(t)=\pm\beta(t+T/2)$ has been found exactly. We have tested the scenario of nonstandard EHC instability with asymmetric driving without the flexoeffect, but were unable to find such an instability with our parameter variation. One possible reason for this is that no matter what the shape of the driving field is, the body force in the linear momentum of the Ericksen-Leslie equations tells us that it will always be out of phase with the driving field, therefore not reinforcing the director fluctuation so no instability happens.

We summarize by saying the a wider variety of observable patterns is possible in light of the nonzero p_c wave numbers that have been calculated for standard EHC for Mischung V and the dielectric instability found in nonstandard EHC under an asymmetric driving field. Finally, some suggestions for future research include using other asymmetric wave forms such as sawtooth excitation along with any influence they might have and a more analytical study on why the dielectric instability only occurs in nonstandard EHC, even though we have director fluctuations both in the subharmonic and dielectric regimes. It would be attractive to find analytical conditions than can cause these conditions to occur or not, similar to the ones found for the simplified 2D model for standard EHC [11].

ACKNOWLEDGMENT

The authors would like to thank Werner Pesch for feedback and suggestions on this paper.

APPENDIX A: MATERIAL PARAMETERS USED

The material parameters for nematics MBBA and Mischung V used in this paper are in Table I, referenced from previous works [10,19–21]. Table II shows the scalings used in order to nondimensionalize the equations.

TABLE I. Parameters and quantities used in the calculation of the stability diagram. Values are nondimensional except for the cell thickness. When using Mischung V with flexoelectricity, we use the MBBA values as a first try.

Quantity	Mischung V values	MBBA values
$\epsilon_\parallel$	5.6	4.72
$\epsilon_\perp$	6	5.25
$\epsilon_a=\epsilon_\parallel-\epsilon_\perp$	−0.4	−0.53
σ_a [a]	0.963	0.500
$\sigma_\perp$	1.926	1.000
α_1	20	−18.1
α_2	−367	−110.4
α_3	0	−1.1
α_4	151	82.6
α_5	282	77.9
α_6	−71	−33.6
γ_1 [b]	367	109.3
$\gamma_2=-\gamma_1$	−367	−109
$\gamma_3=-1/2(\alpha_3+\alpha_6)$	35.5	17.35
$\gamma_4=1/2(\alpha_5-\alpha_2)$	324.5	94.15
$\gamma_5=1/2(\alpha_3+\alpha_6)$	−35.5	−17.35
K_1	14.9	6.66
K_2	6.48	4.2
K_3	13.76	8.61
Cell thickness d	20.2 μm	40 μm
e_1		−3.25
e_3		−4.59

[a]When σ_a is not varied in Sec. III, these values are used.
[b]The Helfrich notation is used here, as opposed to that used by Stewart which would be γ_2 in his book.

APPENDIX B: FULL LINEAR EQUATIONS

The linear equations are derived from the full Ericksen-Leslie dynamic equations (given here in summation notation) [12,22]

TABLE II. Scalings used for nondimensionalization.

Quantity (units)	Mischung V	MBBA
ϵ_0 (F m^{-1})	8.854×10^{-12}	8.854×10^{-12}
α_0 (Pa s)	10^{-3}	10^{-3}
K_0 (N)	10^{-12}	10^{-12}
σ_0 (Ω^{-1} m^{-1})	10^{-12}	10^{-12}
Mass density α_0^2/K_0 (kg m^{-3})	10^{-6}	10^{-6}
Typical length$=d/\pi$ (m)	6.43×10^{-6}	12.73×10^{-6}
$\tau_{DD}=\dfrac{\alpha_0 d^2}{K_0\pi^2}$ (s)	0.0413	0.1621
$V_0=\pi\sqrt{K_0/\epsilon_0}$ (V)	1.0558	1.0558

[4]The asymmetric field nearly becomes a square wave at very high V_l or V_h values.

$$\rho_m \frac{Dv_i}{D\hat{t}} = \rho F_i - (p + w_F)_{,i} + \tilde{g}_j n_{j,i} + G_j n_{j,i} + \tilde{t}_{ij,j}, \quad \text{(B1)}$$

$$\left(\frac{\partial w_F}{\partial n_{i,j}}\right)_{,j} - \frac{\partial w_F}{\partial n_i} + \tilde{g}_i + G_i = \lambda n_i, \quad \text{(B2)}$$

together with the constraint on the director field,

$$\mathbf{n} \cdot \mathbf{n} = 1, \quad \text{(B3)}$$

the equation for continuity,

$$\boldsymbol{\nabla} \cdot \mathbf{v} = 0, \quad \text{(B4)}$$

the quasistatic Maxwell's equations

$$\boldsymbol{\nabla} \cdot \mathbf{D} = \rho_e, \quad \boldsymbol{\nabla} \times \mathbf{E} = \mathbf{0}, \quad \text{(B5)}$$

and an equation describing the dynamics of the current density,

$$\frac{D\rho_e}{D\hat{t}} + \boldsymbol{\nabla} \cdot \mathbf{J} = 0, \quad \text{(B6)}$$

where $\hat{t}$ is normal dimensional time in seconds. This gets nondimensionalized such that $\hat{t} = \tau_{DD} t$.

The nematic energy density w_F is

$$w_F = \frac{1}{2}K_1(\boldsymbol{\nabla} \cdot \mathbf{n})^2 + \frac{1}{2}K_2(\mathbf{n} \cdot \boldsymbol{\nabla} \times \mathbf{n})^2 + \frac{1}{2}K_3(\mathbf{n} \times \boldsymbol{\nabla} \times \mathbf{n})^2 - \frac{1}{2}\epsilon_0\epsilon_a(\mathbf{n} \cdot \mathbf{E})^2 - \mathbf{E} \cdot [e_1\mathbf{n}(\boldsymbol{\nabla} \cdot \mathbf{n}) + e_3(\mathbf{n} \cdot \boldsymbol{\nabla})\mathbf{n}], \quad \text{(B7)}$$

where the first three terms make up the Frank-Oseen elastic energy expression, the last two terms due to the dielectric and flexoelectric effects. The velocity vector $\mathbf{v}$ can be expressed in terms of the poloidal and toroidal velocity potentials f and g [23] by applying the vector operators

$$\left[\frac{\partial^2}{\partial z \partial x}, \frac{\partial^2}{\partial z \partial y}, -\frac{\partial^2}{\partial x^2} - \frac{\partial^2}{\partial y^2}\right] \quad \text{and} \quad \left[\frac{\partial}{\partial y}, -\frac{\partial}{\partial x}, 0\right] \quad \text{(B8)}$$

to Eq. (B1), eliminating the pressure term. So $\mathbf{v}$ becomes

$$\mathbf{v} = \left[\frac{\partial^2}{\partial z \partial x}, \frac{\partial^2}{\partial z \partial y}, -\frac{\partial^2}{\partial x^2} - \frac{\partial^2}{\partial y^2}\right] f + \left[\frac{\partial}{\partial y}, -\frac{\partial}{\partial x}, 0\right] g. \quad \text{(B9)}$$

The stress tensor $\tilde{t}_{ij,j}$ takes the form of Eq. (2.12) in Plaut and Ribetta's paper [24]. This comes from the stress tensor expression with all six Leslie viscosities, applying the Parodi relation

$$\alpha_6 - \alpha_5 = \alpha_2 + \alpha_3 \quad \text{(B10)}$$

and substituting in the viscosities γ_3, γ_4, and γ_5. The electric field is related to the electric potential ϕ by

$$\mathbf{E} = \mathbf{E}_0 - \boldsymbol{\nabla}\phi, \quad \text{(B11)}$$

where $\mathbf{E}_0 = [0, 0, E(t)]$ is the applied electric field. The displacement and current fields $\mathbf{D}$ and $\mathbf{J}$, respectively, are given by the relations

$$\mathbf{D} = \epsilon_0 \underline{\epsilon}\mathbf{E} + e_1\mathbf{n}(\boldsymbol{\nabla} \cdot \mathbf{n}) + e_3(\mathbf{n} \cdot \boldsymbol{\nabla})\mathbf{n}, \quad \text{(B12)}$$

$$\mathbf{J} = \sigma_0 \underline{\sigma}\mathbf{E}, \quad \text{(B13)}$$

where e_1 and e_3 are the flexoelectric coefficients and the conductivity and dielectric tensors, $\underline{\sigma}$ and $\underline{\epsilon}$, respectively, are of the nematic uniaxial form

$$\epsilon_{ij} = \epsilon_\perp \delta_{ij} + \epsilon_a n_i n_j. \quad \text{(B14)}$$

One substitutes the variables of the form in Eqs. (8) and (9) into the equations here and linearize around the basic state:

$$\mathbf{n} = (1,0,0), \quad \mathbf{v} = \mathbf{0}. \quad \text{(B15)}$$

Each linearized equation needs to be multiplied by the appropriate z mode—$S_1(z)$ for the equation containing $\phi_1(t)$, for example—along with a $2/\pi$ factor and integrated from $z = -\pi/2$ to $\pi/2$. This should result in a 10×10 ODE matrix system of the form $\mathcal{D}_0(t;R)\partial_t \mathbf{U}_0(t) = \mathcal{L}(t;R,Q)\mathbf{U}_0(t)$, where

$$\boldsymbol{U}_0(t) = [\phi_1(t), \phi_2(t), n_{y1}(t), n_{y2}(t), n_{z1}(t), n_{z2}(t), f_1(t), f_2(t), g_1(t), g_2(t)]^{\mathsf{T}}. \quad \text{(B16)}$$

The nonzero components of $\mathcal{D}_0$ are

$$[\mathcal{D}_0]_{1,1} = \epsilon_\perp(q^2 + p^2 + 1) + \epsilon_a q^2, \quad \text{(B17)}$$

$$[\mathcal{D}_0]_{1,3} = -\frac{1}{\sqrt{R}} qp(e_1 + e_3), \quad \text{(B18)}$$

$$[\mathcal{D}_0]_{1,5} = iq\epsilon_a E_{\mathrm{ac}}(t), \quad \text{(B19)}$$

$$[\mathcal{D}_0]_{1,6} = -\frac{1}{\sqrt{R}}\frac{8}{3\pi} iq(e_1 + e_3), \quad \text{(B20)}$$

$$[\mathcal{D}_0]_{2,2} = \epsilon_\perp(q^2 + p^2 + 4) + \epsilon_a q^2, \quad \text{(B21)}$$

$$[\mathcal{D}_0]_{2,4} = -\frac{1}{\sqrt{R}} qp(e_1 + e_3), \quad \text{(B22)}$$

$$[\mathcal{D}_0]_{2,5} = \frac{1}{\sqrt{R}}\frac{8}{3\pi} iq(e_1 + e_3), \quad \text{(B23)}$$

$$[\mathcal{D}_0]_{2,6} = iq\epsilon_a E_{\mathrm{ac}}(t), \quad \text{(B24)}$$

$$[\mathcal{D}_0]_{3,3} = [\mathcal{D}_0]_{4,4} = [\mathcal{D}_0]_{5,5} = [\mathcal{D}_0]_{6,6} = \gamma_1, \quad \text{(B25)}$$

$$[\mathcal{D}_0]_{7,4} = qp(\alpha_2 + \alpha_3) I_{7ab}, \quad \text{(B26)}$$

$$[\mathcal{D}_0]_{7,5} = -iq\{\alpha_2(q^2 + p^2) I_{6aa} + \alpha_3 I_{8aa}\}, \quad \text{(B27)}$$

$$[\mathcal{D}_0]_{7,7} = \rho_m\{(q^2 + p^2)^2 - (q^2 + p^2) I_{3aa}\}, \quad \text{(B28)}$$

$$[\mathcal{D}_0]_{8,3} = qp(\alpha_2 + \alpha_3) I_{7ba}, \quad \text{(B29)}$$

$$[\mathcal{D}_0]_{8,6} = -iq\{\alpha_2(q^2 + p^2) I_{6bb} + \alpha_3 I_{8bb}\}, \quad \text{(B30)}$$

$$[\mathcal{D}_0]_{8,8} = \rho_m\{(q^2 + p^2)^2 - (q^2 + p^2) I_{3bb}\}, \quad \text{(B31)}$$

$$[\mathcal{D}_0]_{9,3} = (\alpha_3 p^2 - \alpha_2 q^2), \tag{B32}$$

$$[\mathcal{D}_0]_{9,6} = \frac{8}{3\pi} ip\alpha_3, \tag{B33}$$

$$[\mathcal{D}_0]_{9,9} = -\rho_m(q^2 + p^2), \tag{B34}$$

$$[\mathcal{D}_0]_{10,4} = (\alpha_3 p^2 - \alpha_2 q^2), \tag{B35}$$

$$[\mathcal{D}_0]_{10,5} = -\frac{8}{3\pi} ip\alpha_3, \tag{B36}$$

$$[\mathcal{D}_0]_{10,10} = -\rho_m(q^2 + p^2), \tag{B37}$$

and the non-zero entries for the matrix $\mathcal{L}$ are

$$[\mathcal{L}]_{1,1} = -Q\{\sigma_\perp(q^2 + p^2 + 1) + \sigma_a q^2\}, \tag{B38}$$

$$[\mathcal{L}]_{1,5} = -iQ\sigma_a q E_{\rm ac}(t), \tag{B39}$$

$$[\mathcal{L}]_{2,2} = -Q\{\sigma_\perp(q^2 + p^2 + 4) + \sigma_a q^2\}, \tag{B40}$$

$$[\mathcal{L}]_{2,6} = -iQ\sigma_a q E_{\rm ac}(t), \tag{B41}$$

$$[\mathcal{L}]_{3,1} = -\sqrt{R} qp(e_1 + e_3), \tag{B42}$$

$$[\mathcal{L}]_{3,3} = -(K_1 p^2 + K_3 q^2 + K_2), \tag{B43}$$

$$[\mathcal{L}]_{3,5} = -i\sqrt{R} E_{\rm ac}(t) p(e_1 - e_3), \tag{B44}$$

$$[\mathcal{L}]_{3,6} = -\frac{8}{3\pi} ip(K_1 - K_2), \tag{B45}$$

$$[\mathcal{L}]_{3,8} = qp(\alpha_2 + \alpha_3) I_{2ab}, \tag{B46}$$

$$[\mathcal{L}]_{3,9} = \alpha_3 p^2 - \alpha_2 q^2, \tag{B47}$$

$$[\mathcal{L}]_{4,2} = -\sqrt{R} qp(e_1 + e_3), \tag{B48}$$

$$[\mathcal{L}]_{4,4} = -(K_1 p^2 + K_3 q^2 + 4K_2), \tag{B49}$$

$$[\mathcal{L}]_{4,5} = \frac{8}{3\pi} ip(K_1 - K_2), \tag{B50}$$

$$[\mathcal{L}]_{4,6} = -i\sqrt{R} E_{\rm ac}(t) p(e_1 - e_3), \tag{B51}$$

$$[\mathcal{L}]_{4,7} = qp(\alpha_2 + \alpha_3) I_{2ba}, \tag{B52}$$

$$[\mathcal{L}]_{4,10} = \alpha_3 p^2 - \alpha_2 q^2, \tag{B53}$$

$$[\mathcal{L}]_{5,1} = -iq\epsilon_a R E_{\rm ac}(t), \tag{B54}$$

$$[\mathcal{L}]_{5,2} = -\frac{8}{3\pi} iq\sqrt{R}(e_1 + e_3), \tag{B55}$$

$$[\mathcal{L}]_{5,3} = ip\sqrt{R} E_{\rm ac}(t)(e_1 - e_3), \tag{B56}$$

$$[\mathcal{L}]_{5,4} = -\frac{8}{3\pi} ip(K_1 - K_2), \tag{B57}$$

$$[\mathcal{L}]_{5,5} = \epsilon_a R E_{\rm ac}^2(t) - K_2 p^2 - K_3 q^2 - K_1, \tag{B58}$$

$$[\mathcal{L}]_{5,7} = -iq\{\alpha_2(q^2 + p^2) I_{6aa} + \alpha_3 I_{8aa}\}, \tag{B59}$$

$$[\mathcal{L}]_{5,10} = \frac{8}{3\pi} i\alpha_3 p, \tag{B60}$$

$$[\mathcal{L}]_{6,1} = \frac{8}{3\pi} iq\sqrt{R}(e_1 + e_3), \tag{B61}$$

$$[\mathcal{L}]_{6,2} = -iq\epsilon_a R E_{\rm ac}(t), \tag{B62}$$

$$[\mathcal{L}]_{6,3} = \frac{8}{3\pi} ip(K_1 - K_2), \tag{B63}$$

$$[\mathcal{L}]_{6,4} = ip\sqrt{R} E_{\rm ac}(t)(e_1 - e_3), \tag{B64}$$

$$[\mathcal{L}]_{6,6} = \epsilon_a R E_{\rm ac}^2(t) - K_2 p^2 - K_3 q^2 - 4K_1, \tag{B65}$$

$$[\mathcal{L}]_{6,8} = -iq\{\alpha_2(q^2 + p^2) I_{6bb} + \alpha_3 I_{8bb}\}, \tag{B66}$$

$$[\mathcal{L}]_{6,9} = -\frac{8}{3\pi} i\alpha_3 p, \tag{B67}$$

$$[\mathcal{L}]_{7,1} = RE_{\rm ac}(t)\{\epsilon_\perp(q^2 + p^2)^2 + \epsilon_a q^2(q^2 + p^2)\} I_{6aa} - RE_{\rm ac}(t)\epsilon_\perp(q^2 + p^2) I_{8aa}, \tag{B68}$$

$$[\mathcal{L}]_{7,3} = -\sqrt{R} E_{\rm ac}(t) qp(e_1 + e_3)(q^2 + p^2) I_{6aa}, \tag{B69}$$

$$[\mathcal{L}]_{7,5} = iqRE_{\rm ac}^2(t)\epsilon_a(q^2 + p^2) I_{6aa}, \tag{B70}$$

$$[\mathcal{L}]_{7,6} = iq\sqrt{R} E_{\rm ac}(t)(e_1 + e_3)(q^2 + p^2) I_{7ab}, \tag{B71}$$

$$[\mathcal{L}]_{7,7} = -\left\{\frac{1}{2}\alpha_4(q^2 + p^2) + \gamma_4 q^2\right\}(q^2 + p^2)^2 + \{\alpha_1 q^4 + \alpha_4(q^2 + p^2)^2 + (\gamma_4 - \gamma_3) q^2(q^2 + p^2)\} I_{3aa} + \left\{\gamma_3 q^2 - \frac{1}{2}\alpha_4(q^2 + p^2)\right\} I_{5aa}, \tag{B72}$$

$$[\mathcal{L}]_{7,10} = qp[\alpha_1 q^2 - \gamma_3(q^2 + p^2)] I_{7ab} + qp\gamma_3 I_{9ab}, \tag{B73}$$

$$[\mathcal{L}]_{8,2} = RE_{\rm ac}(t)\{[\epsilon_\perp(q^2 + p^2)^2 + \epsilon_a q^2(q^2 + p^2)] I_{6bb} - \epsilon_\perp(q^2 + p^2) I_{8bb}\}, \tag{B74}$$

$$[\mathcal{L}]_{8,4} = -\sqrt{R} E_{\rm ac}(t) qp(e_1 + e_3)(q^2 + p^2) I_{6bb}, \tag{B75}$$

TABLE III. Values for the various I terms in matrices $\mathcal{D}_0$ and $\mathcal{L}$ as a result of projecting the linear equations onto the z modes.

Coefficient	Inner Product	Numerical value
I_{2ab}	$\langle S_1(z)\vert\frac{d}{dz}C_2(z)\rangle$	0.73984
I_{2ba}	$\langle S_2(z)\vert\frac{d}{dz}C_1(z)\rangle$	1.11187
I_{3aa}	$\langle C_1(z)\vert\frac{d^2}{dz^2}C_1(z)\rangle$	−1.24652
I_{3bb}	$\langle C_2(z)\vert\frac{d^2}{dz^2}C_2(z)\rangle$	−4.66589
I_{4ab}	$\langle S_1(z)\vert\frac{d^3}{dz^3}C_2(z)\rangle$	−0.73984
I_{4ba}	$\langle S_2(z)\vert\frac{d^3}{dz^3}C_1(z)\rangle$	−4.44750
I_{5aa}	$\langle C_1(z)\vert\frac{d^4}{dz^4}C_1(z)\rangle$	5.13877
I_{5bb}	$\langle C_2(z)\vert\frac{d^4}{dz^4}C_2(z)\rangle$	39.04725
I_{6aa}	$\langle C_1(z)\vert S_1(z)\rangle$	0.98624
I_{6bb}	$\langle C_2(z)\vert S_2(z)\rangle$	−0.97642
I_{7ab}	$\langle C_1(z)\vert\frac{d}{dz}S_2(z)\rangle$	−1.11187
I_{7ba}	$\langle C_2(z)\vert\frac{d}{dz}S_1(z)\rangle$	−0.73984
I_{8aa}	$\langle C_1(z)\vert\frac{d^2}{dz^2}S_1(z)\rangle$	−0.98624
I_{8bb}	$\langle C_2(z)\vert\frac{d^2}{dz^2}S_2(z)\rangle$	3.90568
I_{9ab}	$\langle C_1(z)\vert\frac{d^3}{dz^3}S_2(z)\rangle$	4.44748
I_{9ba}	$\langle C_2(z)\vert\frac{d^3}{dz^3}S_1(z)\rangle$	0.73984

$$[\mathcal{L}]_{8,5} = iq\sqrt{R}E_{\mathrm{ac}}(t)(e_1+e_3)(q^2+p^2)I_{7ba}, \tag{B76}$$

$$[\mathcal{L}]_{8,6} = iqRE_{\mathrm{ac}}^2(t)\epsilon_a(q^2+p^2)I_{6bb}, \tag{B77}$$

$$[\mathcal{L}]_{8,8} = -\left\{\frac{1}{2}\alpha_4(q^2+p^2)+\gamma_4 q^2\right\}(q^2+p^2)^2 + \{\alpha_1 q^4+\alpha_4(q^2+p^2)^2+(\gamma_4-\gamma_3)q^2(q^2+p^2)\}I_{3bb} + \left\{\gamma_3 q^2-\frac{1}{2}\alpha_4(q^2+p^2)\right\}I_{5bb}, \tag{B78}$$

$$[\mathcal{L}]_{8,9} = qp[\alpha_1 q^2-\gamma_3(q^2+p^2)]I_{7ba}+qp\gamma_3 I_{9ba}, \tag{B79}$$

$$[\mathcal{L}]_{9,8} = -qp\{[-\alpha_1 q^2+\gamma_3(q^2+p^2)]I_{2ab}-\gamma_3 I_{4ab}\}, \tag{B80}$$

$$[\mathcal{L}]_{9,9} = \left[\frac{1}{2}\alpha_4(q^2+p^2+1)+\gamma_4 q^2-\gamma_3 p^2\right](q^2+p^2) + \alpha_1 q^2p^2-\gamma_3 p^2, \tag{B81}$$

$$[\mathcal{L}]_{10,7} = -qp[-\alpha_1 q^2+\gamma_3(q^2+p^2)]I_{2ba}+qp\gamma_3 I_{4ba}, \tag{B82}$$

$$[\mathcal{L}]_{10,10} = \left[\frac{1}{2}\alpha_4(q^2+p^2+4)+\gamma_4 q^2-\gamma_3 p^2\right](q^2+p^2) + \alpha_1 q^2p^2-4\gamma_3 p^2, \tag{B83}$$

where the I's are the numerical coefficients of the inner products of the form

$$\langle h\vert\hat{h}\rangle = \frac{2}{\pi}\int_{z=-\pi/2}^{z=\pi/2} h(z)\hat{h}(z)dz, \tag{B84}$$

given in Table III. Here, there is no $\partial_t E_{\mathrm{ac}}$ term in the matrices since they are zero for a piecewise constant field such as Fig. 1. Equation (10) can be obtained by setting $\rho_m=0$ and therefore eliminating f and g.

APPENDIX C: THE SWITCHING MATRICES

For the simple linear model with a piecewise constant electric field $E_{\mathrm{ac}}(t)$ used by John and Stannarius [10], the evolution of the variables in time can be calculated by a series of matrix exponentials acting on the initial conditions. We do the same, as shown by Eqs. (12) and (13); however, since we use the electric potential ϕ rather than the charge density ρ_e, we need to insert these "switching" matrices into the chain since ϕ jumps discontinuously at the points where the piecewise-constant field $E_{\mathrm{ac}}(t)$ jumps as well. These switching matrices are calculated where all the variables except ϕ are the same at either side of the jump so that (for a 3×3 system)

$$\underline{\mathbf{G}}_{\mathrm{after}}\begin{pmatrix}\phi_{\mathrm{after}}\\ n_y\\ n_z\end{pmatrix} = \begin{pmatrix}\phi_{\mathrm{before}}\\ n_y\\ n_z\end{pmatrix}\underline{\mathbf{G}}_{\mathrm{before}}, \tag{C1}$$

i.e.,

$$\begin{pmatrix}\phi_{\mathrm{after}}\\ n_y\\ n_z\end{pmatrix} = \underbrace{\underline{\mathbf{G}}_{\mathrm{after}}^{-1}\underline{\mathbf{G}}_{\mathrm{before}}}_{\underline{\mathbf{S}}}\begin{pmatrix}\phi_{\mathrm{before}}\\ n_y\\ n_z\end{pmatrix}, \tag{C2}$$

where the subscript "after" is associated with the value of the electric field after the jump and vice versa. The $\underline{\mathbf{G}}$ matrices can be derived from the charge equation [Eq. (B5)].

[1] *Pattern Formation in Liquid Crystals*, edited by A. Buka and L. Kramer (Springer-Verlag, New York, 1996).
[2] A. Buka, N. Éber, W. Pesch, and L. Kramer, Phys. Rep. **448**, 115 (2007).
[3] A. Buka, N. Éber, and W. Pesch, in *Self-assembly, Pattern Formation and Growth Phenomena in Nano-systems*, edited by A. A. Golovin and A. A. Nepomnyashchy (Springer, New York, 2006), pp. 55–82.
[4] E. F. Carr, Mol. Cryst. Liq. Cryst. **7**, 253 (1969).
[5] W. Helfrich, J. Chem. Phys. **51**, 4092 (1969).
[6] P. G. de Gennes, E. Dubois-Violette, and O. Parodi, J. Phys. (Paris) **32**, 305 (1971).
[7] E. Dubois-Violette, J. Phys. (Paris) **33**, 95 (1972).
[8] S. T. Langerwall, E. Dubois-Violette, I. W. Smith, Y. Galerne, and G. Durand, J. Phys. (Paris), Colloq. **36**, C1-237 (1975).
[9] A. Krekhov, W. Pesch, N. Éber, T. Toth-Katona, and A. Buka, Phys. Rev. E **77**, 021705 (2008).
[10] T. John and R. Stannarius, Phys. Rev. E **70**, 025202(R) (2004).
[11] R. Stannarius, J. Heuer, and T. John, Phys. Rev. E **72**, 066218 (2005).
[12] I. W. Stewart, *The Static and Dynamic Continuum Theory of Liquid Crystals* (Taylor & Francis, London, 2004).
[13] T. John, J. Heuer, and R. Stannarius, Phys. Rev. E **71**, 056307 (2005).
[14] S. Chandrasekhar, *Liquid Crystals* (Cambridge University Press, Cambridge, England, 1992), Chap. 3, pp. 187–189.
[15] E. Plaut and W. Pesch, Phys. Rev. E **59**, 1747 (1999).
[16] M. Kaiser and W. Pesch, Phys. Rev. E **48**, 4510 (1993).
[17] S. Chandrasekhar, *Hydrodynamic and Hydromagnetic Stability* (Oxford University Press, Oxford, 1961).
[18] E. Bodenschatz, W. Zimmermann, and L. Kramer, J. Phys. (Paris) **49**, 1875 (1988).
[19] W. Decker, Diploma, University of Bayreuth, 1990.
[20] J. Shi, C. Wang, V. Surendranath, K. Kang, and J. T. Gleeson, Liq. Cryst. **29**, 877 (2002).
[21] R. Stannarius (personal communication).
[22] S. J. Tavener, T. Mullin, G. I. Blake, and K. A. Cliffe, Phys. Rev. E **63**, 011708 (2000).
[23] F. H. Busse and E. W. Bolton, J. Fluid Mech. **146**, 115 (1984).
[24] E. Plaut and R. Ribotta, Eur. Phys. J. B **5**, 265 (1998).